Doctor-Blade Casting Fabrication of Ultrathin Li Metal Electrode for High-Energy-Density Batteries

*Junmou Du, Wenyu Wang, Mintao Wan, Xiancheng Wang, Guocheng Li, Yucheng Tan, Chunhao Li, Shuibin Tu, and Yongming Sun**

The employment of ultrathin Li metal electrodes with matched capacity with current cathodes and improved electrochemical stripping/plating behaviors plays a key role in the realization of high-energy-density batteries. However, their fabrication remains challenging using regular cold rolling processing due to inferior processibility of metallic Li. Herein, a facile molten metal doctor-blade casting approach is explored to fabricate uniform metallic Li layers with thickness ranging from 10 to 50 µm on regular battery Cu current collectors with a lithiophilic Sn interphase layer. The enhanced surface wettability between Li and the spontaneously formed Li–Sn alloy helps to realize uniform spreading, and formation of an ultrathin and uniform metallic Li layer. The existence of the Li–Sn alloy in the bulk of metallic Li electrode helps to reduce the nucleation barrier and improve the electrochemical performance of the Li metal. With a cathode areal capacity of 2.8 mA h cm^{-2} the LiCoO$_2$||Li/Li–Sn full cell shows improved capacity retention from 58% to 77% after 100 cycles at a lower Negative/Positive ratio of 2/1, offering a high energy density of 662.4 W h kg^{-1}. The enhanced electrochemical performance of the as-fabricated ultrathin Li metal electrode with high energy density opens up a promising pathway for realizing next-generation high-energy-density batteries.

1. Introduction

Lithium-ion batteries (LIBs) have been widely used in consume electronics, electric vehicles, and are being penetrated into power grids.[1] Currently, the increase in battery energy density becomes urgent to meet the goal set for longer driving range of electromobiles and battery standby time for mobiles. However, the energy density of traditional LIBs is reaching their theoretical value, the pursue of higher energy density requires new battery chemistry beyond the state-of-art battery technology, such as using alloy-type Si based anode or stripping/plating-type lithium (Li) metal anode to replace intercalation-type graphite anode in commercial lithium-ion batteries.[2] Li metal delivers 10 times higher theoretical specific capacity than current graphite (3860 mA h g^{-1} for metallic Li versus 372 mA h g^{-1} for graphite) and lowest redox voltage (−3.04 V versus standard hydrogen electrode) among all the anodes, exhibiting great promise as high-performance anode in the next-generation high-energy-density lithium-based rechargeable batteries.[3] Nevertheless, nearly infinite volume expansion/shrinkage and inhomogeneous stripping/plating behavior lead to the growth of dendritic behaviors of metallic Li, which would cause short circuits and other safety issues.[3b,4] Accompanied by large volume change, repeated fracture and repair of solid electrolyte interface (SEI) occurs during the charge/discharge processes, which causes continuous consumption of active lithium and electrolyte, and finally inferior cycling stability.[5] Recently, extensive studies on electrode surface protection, composite structure, and electrolyte engineering have been conducted to improve the cycle life and safety hazards of metallic Li electrode.[6] However, highly overloaded lithium metal anodes (e.g., 500 µm for ≈100 mA h cm^{-2}) and flooding amount of electrolytes were often employed for the evaluation of electrochemical performance of metallic Li. The use of thick Li metal anodes and excessive electrolyte does not support high energy density of batteries and are not feasible in practical applications. Therefore, high-performance ultrathin lithium metal anodes (e.g., 10–50 µm) that possess matched capacities with current cathodes are of key importance to practical battery application. However, the high homologous temperature (T_h, for metallic lithium, T_h is 0.66 at room temperature) of metallic Li at room temperature leads a strong influence of diffusion creep on its deformation,[7] and the resulting sticky nature and poor mechanical processability make it challenging to realize large-scale fabrication of ultrathin pure Li metal electrode by regular mechanical rolling operation.

Free-standing ultrathin metallic Li foil cannot sustain operation for battery fabrication and large current in real application condition, it is of great importance for the employment of current collector with high conductivity and mechanical durability for the practical implantation of ultrathin metallic Li anode in high-energy-density batteries, which is similar to metal current collector for traditional porous electrodes (e.g., graphite on Cu foil). Cu foil is lithiophobic to molten lithium, which

---

J. Du, W. Wang, M. Wan, X. Wang, G. Li, Y. Tan, C. Li, S. Tu, Y. Sun
Wuhan National Laboratory for Optoelectronics (WNLO)
Huazhong University of Science and Technology
Wuhan, China
E-mail: yongmingsun@hust.edu.cn

The ORCID identification number(s) for the author(s) of this article can be found under https://doi.org/10.1002/aenm.202102259.

DOI: 10.1002/aenm.202102259

causes difficulty in preparing ultrathin metallic Li electrode on it by slurry doctor-blade casting approach.[8] Till now, there have been few reports taking the direction of fabrication of ultrathin metallic Li on Cu foil with superior electrochemical performance for advanced Li metal batteries. It is revealed that formation of chemical bonds through functional organic coatings on Cu foil can improve the wettability of molten lithium, providing great opportunities to spread metallic Li.[9] Since ultrathin Li layer can be peeled off due to the organic coatings derived interphase, one has to construct tightly coupling structure between metallic Li and current collector for large-scale fabrication and application of ultrathin metallic Li electrode in future studies. Some metals (e.g., Sn, Zn, In, Ag, and Al) react easily with metallic Li, producing lithium alloys, and showing good wettability to molten lithium.[8a,10] Also, these lithium alloys usually possess large chemical diffusion coefficient, which decreases the energy barrier of Li diffusing and spontaneously drives the fast lithium transfer from Li-rich phase to Li-poor phase.[11] Hence, molten Li can easily spread on the surface of these lithium alloys and form a homogeneous lithium layer. From this respect, a thin lithiophilic metal interphase with good contact with the substrate may be a good choice to realize close contact between metallic Li and Cu foil. On the other hand, low loading of pure ultrathin metallic Li anode often exhibits inferior electrochemical performance, including insufficient cycling, low Coulombic efficiency (CE), and dendritic lithium deposition. Lithiophilic metal substrate can help to improve electrochemical performance of metallic Li electrode.[10f,12] Lithium nucleation usually shows lower overpotential on lithiophilic metal substrate. Owing to the strong interactions of metallic Li to lithiophilic metals, metallic Li is inclined to nucleate on the alloy (e.g., $Li_{22}Sn_5$ and Li_9Al_4) sites, leading to low nucleation barrier.[10b,e,f,12a] Importantly, lithiophilic surface can also homogenize the lithium deposition and reduce the risk of formation of hazardous lithium dendrites. The uniform electrochemical lithium plating/stripping behavior is also helpful for long cycling lifespan. So far, alloying strategy has been widely reported in various battery systems.[13] Therefore, the introduction of lithiophilic metal and its spontaneous formation of lithium alloy could not only help to form a uniform ultrathin metallic Li layer on current collector with close contact, but also improve the electrochemical performance.

In this work, a facile doctor-blade casting strategy was successfully explored to construct a large-size ultrathin lithium metal electrode on Cu collector with a lithiophilic metal interphase for high-energy-density and long-life rechargeable batteries. With a superficial lithiophilic Sn layer, molten lithium spreads uniformly on commercial Cu current collector with close contact during blade casting operation and forms a homogeneous metal Li layer with controlled thickness. The introduction of Sn layer (≈0.2 mg cm^{-2}) on Cu current collector significantly enhances the wettability to molten Li, and helps it spread uniformly and form close contact with Cu current collector. The thin Sn layer reacts with metallic Li and diffuse into the bulk lithium matrix, forming a Li–Sn alloy uniformly dispersed ultrathin Li electrode. By controlling the amount of Li, the areal capacity of the as-fabricated metallic Li electrode is precisely adjusted from 2 to 10 mA h cm^{-2} (corresponding to thickness from 10 to 50 μm). The Li–Sn alloy functions as lithiophilic site, significantly reduces the electrochemical nucleation barrier of metallic Li, regulates the lithium plating/stripping behavior, and thus alleviates the dendritic growth of metallic Li and improves the CE. As expected, Li||Li symmetric cell with such ultrathin Li metal electrode showed stable plating/striping cycling of over 900 h and lower over-potential (≈11 mV) at 1 mA cm^{-2} and 1 mA h cm^{-2}, in comparison to 380 h for the counterpart with bare Li metal electrode. By pairing such ultrathin Li metal anode with $LiCoO_2$ cathode, the full cell exhibited high energy density of 662.4 W h kg^{-1} and enhanced cycling stability at a low Negative/Positive ratio (N/P ratio) of 2/1. This work explores the possibility of construction of ultrathin metallic Li electrode using a facile doctor-blade casting approach for high-energy-density rechargeable batteries.

2. Results and Discussions

A lithiophilic Sn interfacial layer was first constructed on Cu current collector before the preparation of ultrathin Li metal electrode. The ultrathin Li metal electrode was readily fabricated by spreading molten Li on Cu/Sn surface at 200 °C using a doctor blade, as illustrated in **Figure 1**a. After magnetron sputtering of ultrathin Sn nanolayer, the color of bare Cu foil turned from brown to gray (Figure S1, Supporting Information). The scanning electron microscopy (SEM) images of the Cu/Sn foil showed an ultrathin and dense Sn nanolayer with a mass loading of 0.2 mg cm^{-2}, which was tightly adhered to the Cu surface (Figure S2, Supporting Information). The wettability between molten lithium and Cu/Sn was investigated. As shown in Figure 1b, the molten Li could spontaneously spread on the surface of Cu/Sn in seconds (Figure 1c and Figure S3, Supporting Information), indicating the good wettability to molten Li. In contrast, a large contact angel between molten lithium and bare Cu was observed, suggesting its poor wettability to molten Li. Thus, ultrathin Li metal electrode could be readily fabricated by spreading molten Li on the lithiophilic Sn surface at 200 °C using a doctor blade. In our experiment, an ultrathin Li–Sn electrode with large size of 40 cm^2 was easily realized (Figure 1d and Figure S4, Supporting Information). The ultrathin Li–Sn presented a dense and uniform distribution on the Cu foil, showing uniform thickness of 25 μm as demonstrated by SEM image (Figure 1e). Note that there was no gaps/pores between the Cu current collector and metallic Li layer, showing the close contact between the active materials (metallic Li here) and current collector (Cu foil here). CE and nucleation overpotential of Li deposition on Cu and Cu/Sn were studied. As shown in Figure S5 (Supporting Information), Cu/Sn electrode showed much lower nucleation overpotential (73 mV) compared to bare Cu (170 mV). The Cu/Sn also exhibited superior cycling performance of up to 250 cycles with an average CE of 95%, indicating its good lithiophilic nature of Sn to lithium. Once the contact between molten Li and Sn, alloying reaction took place to form lithiophilic Li–Sn alloy, the molten lithium spread easily on the as-formed Li–Sn alloy. Some Li–Sn alloy particles may diffuse into the bulk of thin metallic Li layer, forming ultrathin composite lithium metal electrode. An area capacity of 4.7 mA h cm^{-2} was extracted for the as-fabricated 25 μm Li/Li–Sn electrode, corresponding to

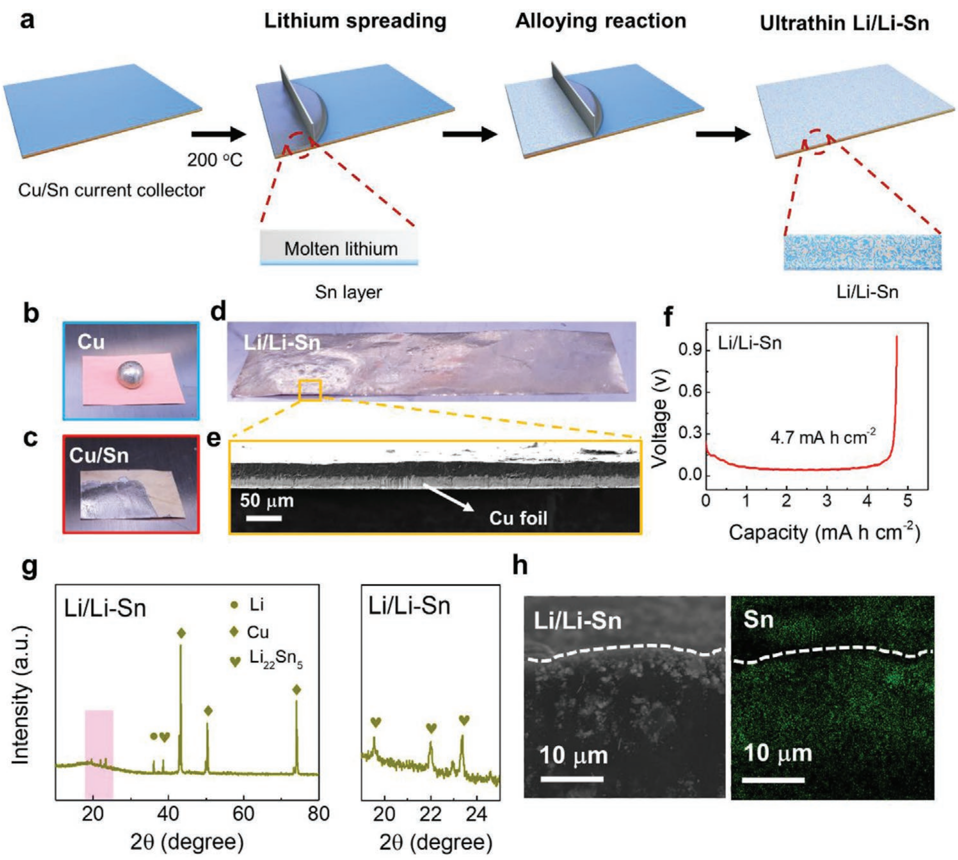

Figure 1. a) Schematic of the fabrication process of ultrathin Li/Li–Sn electrode. Digital photos of molten Li on b) Cu foil and c) Sn coated Cu foil at 200 °C. d) Photograph of the as-prepared Li/Li–Sn electrode. e) Cross-section SEM image of the ultrathin Li/Li–Sn electrode. f) Electrochemical Li stripping curve of the ultrathin Li/Li–Sn electrode. g) XRD pattern of the Li/Li–Sn electrode. h) Cross-section SEM and the corresponding Sn EDS mapping images of ultrathin Li/Li–Sn electrode.

a high specific capacity up to 3300 mA h g^{-1} due to the low content of Sn (Figure 1f). The thickness and areal capacity of Li/Li–Sn electrode can be regulated by adjusting the gap size between the doctor blade and Cu/Sn foil. For example, an ultrathin electrode of 10 µm (2 mA h cm^{-2}) was readily fabricated (Figure S6, Supporting Information). This ultrathin Li/Li–Sn electrode exhibited superior flexibility and mechanical strength (Figure S7, Supporting Information), which was practical for large-scale electrode processing and battery fabrication. The phase information of the Li/Li–Sn electrode was investigated by X-ray diffraction (XRD) measurements. As shown in Figure 1g, all the XRD peaks for the sample were indexed to metallic Li, $Li_{22}Sn_5$, and Cu. The intensive peak at 36.2° corresponded to (110) plane of metallic Li. The peaks at 19.5°, 22.0°, 23.4°, and 38.7° could be attributed to $Li_{22}Sn_5$, indicating the complete alloying reaction of Sn. The cross-section SEM image of Li/Li–Sn electrode clearly showed that Li–Sn alloy particles were uniformly distributed on the surface and the entire electrode (Figures S8 and S9, Supporting Information). SEM and the corresponding energy dispersive X-ray spectroscopy (EDS) mapping images further (Figure 1h) confirmed the uniform distribution of Sn element over the entire metallic Li electrode, indicating the diffusion of Sn species from bottom (the surface of Cu foil) to the bulk of metallic Li under heating conditions. The unique structure of Li/Li–Sn electrode provided abundant lithiophilic sites that could induce uniform lithium plating/stripping process. Moreover, this method can be readily extended to other metals such as Al, Zn, Ag, and In to construct lithiophilic current collectors. The above results indicate that ultrathin metallic Li electrodes with controlled capacities/thicknesses can be fabricated on Cu current collectors with lithiophilic metal (or lithium-alloy) nanolayer.

The electrochemical performance of ultrathin Li/Li–Sn electrode was measured by symmetric cell configuration at different current densities in ether-based electrolyte. The cells were evaluated at a fixed capacity of 1 mA h cm^{-2}, corresponding to a charge/discharge depth of 20%. The ultrathin Li–Sn exhibited stable voltage polarization with an average overpotential of about 12 mV even after 900 h. As for the pure Li electrode, the voltage fluctuated violently and the overpotential became higher than 500 mV after 150 cycles (**Figure 2**a–c), indicating unstable lithium plating/stripping behavior and fast electrochemical performance decay. The ultrathin Li/Li–Sn electrode with thickness of 25 µm even showed better electrochemical performance than pure Li electrode with thickness of 250 µm. As shown in Figure S10 (Supporting Information), the thick pure Li electrode showed an average overpotential of 18 mV, which was higher than 12 mV for the ultrathin Li–Sn electrode. The voltage polarization of the thick Li electrode began to increase gradually after 700 h. By contrast, the

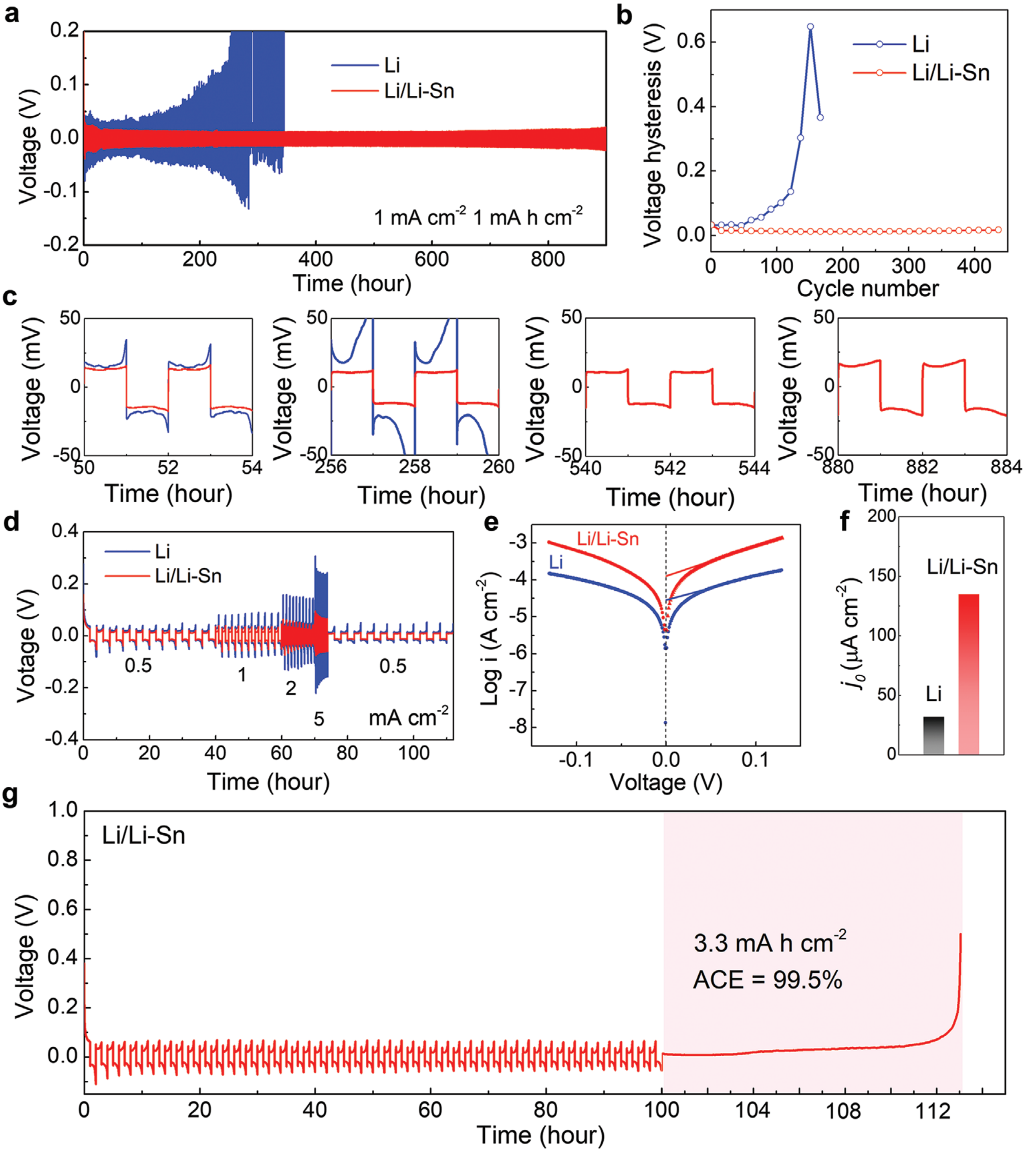

Figure 2. a) Lithium stripping/plating cycling of symmetric cells with ultrathin Li/Li–Sn and bare Li (25 µm) electrodes at 1 mA cm^{-2} and b) the corresponding voltage hysteresis. c) Voltage profiles of Li/Li–Sn and Li symmetric cells. d) Voltage profiles of symmetric cells at different current densities from 0.5 to 5 mA cm^{-2} with a fixed capacity of 1 mA h cm^{-2}. e) Tafel plots of bare Li and Li/Li–Sn symmetric cells and f) calculated exchange current density. g) The ACE of Li/Li–Sn||Li/Li–Sn cell for 50 lithium plating/stripping cycles at 1 mA cm^{-2} and 1 mA h cm^{-2}.

polarization of ultrathin Li/Li–Sn electrode remained stable on cycling, which exhibited superior cycling stability. The superior electrochemical performance of ultrathin Li/Li–Sn electrodes with different thicknesses was also confirmed in cells using corrosive carbonate electrolyte. As shown in Figure S11 (Supporting Information), Li/Li–Sn electrodes with thicknesses of 15, 25, and 50 µm exhibited much more stable cycling than bare Li electrodes with the same thicknesses cycled under

1 mA cm^{-2} and 1 mA h cm^{-2}. Further electrochemical measurements of Li/Li–Sn electrodes were conducted at different rates at a fixed areal capacity of 1 mA h cm^{-2}. As shown in Figure 2d, the voltage hysteresis of 25 µm-thick ultrathin Li/Li–Sn electrode was 23 mV at 2 mA cm^{-2}, which was lower than the controlled bare Li electrode (46 mV). With the increase of the current density to 5 mA cm^{-2}, the overpotential for the bare Li||Li cell sharply increased to 95 mV, while the cell with Li/Li–Sn electrode only showed a relatively slow increase to 43 mV. This result indicated that Li/Li–Sn electrode possesses enhanced electrochemical cycling performance and fast reaction kinetics.

The role of Sn in Li/Li–Sn electrode on the cycling performance of symmetric cells was further investigated. To compare the reaction kinetics at the interface of the Li/Li–Sn electrode and bare Li electrode, the exchange current densities of the Li/Li–Sn and the bare Li electrodes were measured. When the concentration polarization is negligible, the exchange current density can be calculated based on Tafel equation.

$$\eta = a + b\log\left(j\right) \tag{1}$$

where j is the current density, η is the overpotential, a and b are constants.

As shown in Figure 2e,f, the exchange current density of the Li–Sn electrode is 135 µA cm^{-2}, which was much higher than 32 µA cm^{-2} for the bare Li electrode. According to Butler–Volmer equation, the higher exchange current density could decrease the electrochemical polarization of Li/Li–Sn electrode, which was consistent with our result (Figure 2d). The faster charge transfer at the electrode/electrolyte interface can efficiently improve the electrochemical reaction kinetics.[14] The improved exchange current density can be attributed to the uniformly dispersed Li–Sn sites, the Li–Sn alloys with high Li$^+$ conductivity can decrease the nucleation barrier of lithium, and induce uniform lithium deposition with low overpotential. Considering the limited areal capacity of pure ultrathin Li electrode (e.g., ≈ 5 mA h cm^{-2}), it is of great significance to realize high CE in consideration of long-term cycling application. The average Coulombic efficiency (ACE) for Li plating/stripping cycling of 25 µm-thick Li/Li–Sn electrode was measured. As shown in Figure 2g, the Li/Li–Sn electrode exhibited an excellent ACE of 99.5% after 100 h at a current density of 1 mA cm^{-2}, which was higher than of 25 µm bare Li (98.4%, Figure S12, Supporting Information). Therefore, the introduction of Li–Sn species homogenizes the lithium plating/stripping behavior, improves the CE, and prolongs cycling lifespan of the electrodes.

The morphology of Li/Li–Sn electrode after different Li plating/stripping cycling was characterized by SEM. As shown in **Figure 3**a, after the initial lithium plating, the surface of the bare Li electrode showed a loosely arranged and needle-like morphology, which brought the potential risk of internal short circuit. After Li plating/stripping 50 cycles, the bare Li electrode exhibited a rough surface structure with lots of pores and cracks, suggesting aggravated nonuniform lithium deposition and quick electrode degradation (Figure 3b and Figure S13a, Supporting Information). Such Li plating/stripping processes would lead to the continuous exposure of fresh Li to electrolyte and cause continuous side reactions between them upon cycling. Random Li deposition and their dissolution behaviors, together with the accumulated side products during cycling, produced loose stacking layer on the electrode over cycling. As shown by cross-section SEM image, the thickness of such porous layer reached ≈31 µm for the bare Li metal electrode (Figure 3c), This thick and porous layer would seriously block the ionic and electrical connections, suppress the mass transfer, and significantly increase the internal resistance. In contrast, compactly stacked lithium grains with large size of ≈10 µm were uniformly deposited on the Li/Li–Sn surface after initial plating (Figure 3d), indicating the great role of Li–Sn alloy in regulating the uniform lithium nucleation and deposition. After 50 Li plating/stripping cycles, a dense lithium layer instead of dendritic growth was observed on the surface of Li/Li–Sn electrode, showing the stable electrochemical Li plating/stripping behaviors (Figure 3e and Figure S13b, Supporting Information). The dense structure of the Li/Li–Sn electrode after cycling was also confirmed by the results of cross-section SEM measurements and no obvious pores were observed for the Li/Li–Sn electrode (Figure 3f). As shown in Figure S14 (Supporting Information), loose structure with abundant dendrites were formed on the surface of pure Li electrode after 100 cycles, and large cavities and even cracks were clearly observed after 200 cycles, suggesting its nonuniform lithium deposition behavior and fast electrode degradation. In contrast, the Li/Li–Sn electrode showed a flat and compact surface after 200 cycles, indicating the important role of Li–Sn alloy in regulating the lithium metal plating/stripping behavior and improving the electrochemical performance. The dense electrochemical deposition behavior suppresses the side reactions between active metallic Li and electrolyte, which is beneficial for improving CE and cycling. As is shown in Figure 3g and Figure S15 (Supporting Information), Nyquist plots of Li/Li–Sn and bare Li electrode were performed to probe the interfacial impedance after different cycles at 1 mA cm^{-2}. The semicircle at high frequency regions in the Nyquist plots was attributed to the impedance of SEI film (R_{SEI}). The R_{SEI} of the cell with Li/Li–Sn electrode was about 20 Ω after 50 cycles. In contrast, the Li electrode possessed a larger R_{SEI} of 32 Ω. This result again supports that the Li–Sn species facilitate the lithium transfer at the electrode/electrolyte interface. The element distribution of Li/Li–Sn electrode after cycling was measured. EDX mapping results showed that Sn element was uniformly distributed in the lithium matrix after 50 cycles (Figure S16, Supporting Information), indicating Li–Sn alloys remained uniformly distributed in the electrode even after repeated Li plating/stripping cycling. The improvements in plated Li morphology can be generally explained by the faster lithium diffusion in the Li/Li–Sn electrode. The lithium diffusion coefficient on Li–Sn alloy was determined by galvanostatic intermittent titration technique (GITT). As shown in Figure S17 (Supporting Information), Li–Sn alloy showed a lithium diffusion coefficient level of 10^{-12}–10^{-11} cm^{-2} s^{-1}, much higher than the bare metallic lithium.[11] Based on the faster diffusion rate on Li/Li–Sn electrode, the lithium atom can rapidly diffuse across the Li/Li–Sn surface and form a smooth Li plating layer, while the slow diffusion of Li on bare Li electrode induces the vertical growth of deposited lithium, and eventually leads to the dendrite formation. The composition of the SEI was investigated by X-ray photoelectron

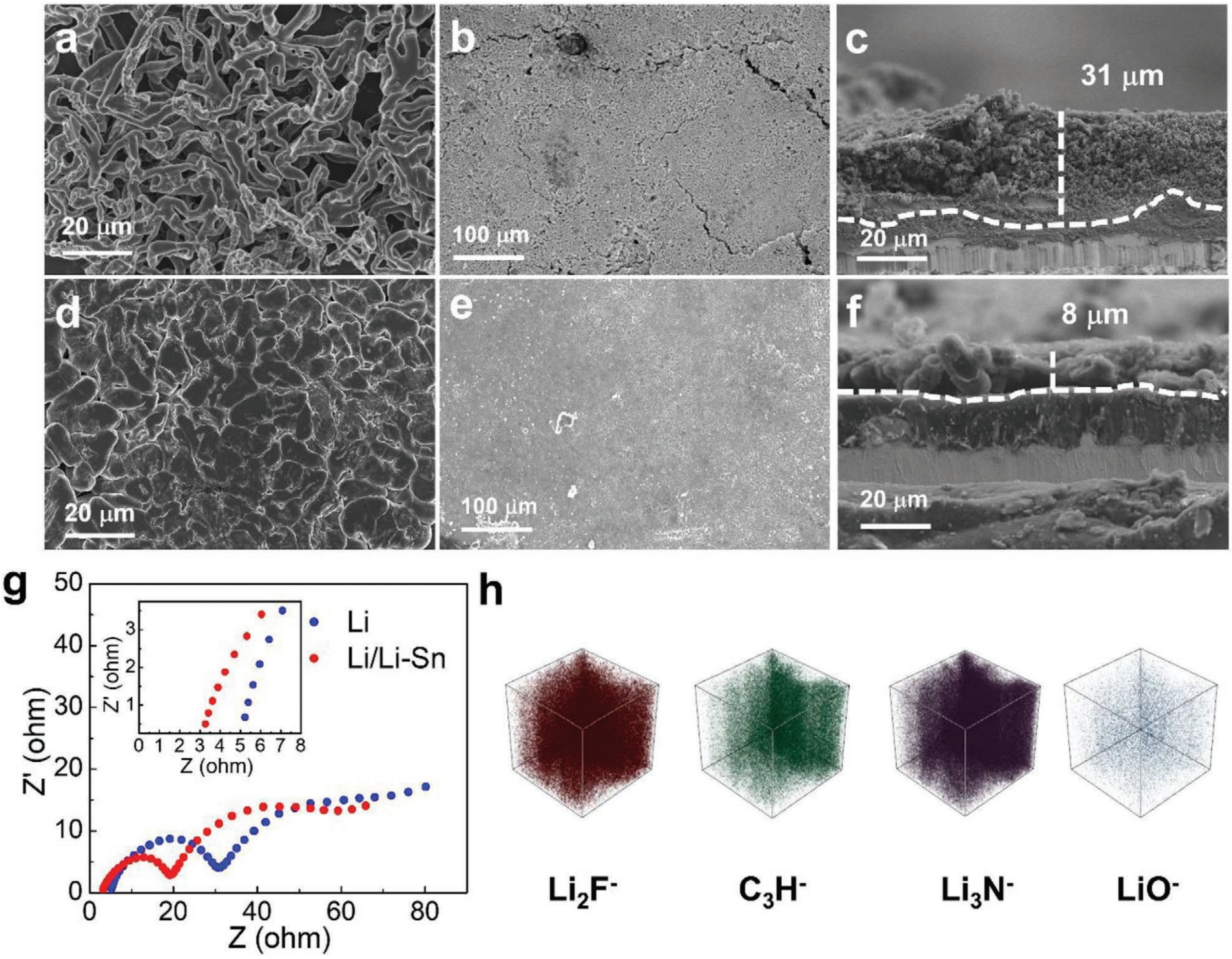

Figure 3. Morphology changes of the bare Li and Li/Li–Sn electrodes after cycling by testing Li||Li and Li/Li–Sn||Li/Li–Sn symmetric cells at 1 mA cm^{-2} and 1 mA h cm^{-2}. a) Top-view SEM image of the bare Li electrode after the first lithium plating. b) Top-view and c) cross-section SEM images of the bare Li electrode after 50 cycles. d) Top-view SEM image of the Li/Li–Sn electrode after the first lithium plating. e) Top-view and f) cross-section SEM images of the Li/Li–Sn electrode after 50 cycles. g) EIS spectra of Li||Li and Li/Li–Sn||Li/Li–Sn symmetric cells after 50 plating/stripping cycles. h) 3D structure views for TOF-SIMS depth sputtering on the surface of Li/Li–Sn after 50 plating/stripping cycles.

spectroscopy (XPS). The result of high-resolution F 1s spectrum suggested that the SEI film contained plentiful LiF (685.5 eV, Figure S18, Supporting Information). Weak information of Li_2CO_3 (55.2 eV) and LiOH (54.8 eV) was also observed in the high-resolution Li 1s spectra.[10a,15] These inorganics afforded strong mechanical strength and good ionic conductivity that could homogenize the lithium plating/stripping behavior. Furthermore, the SEI composition of cycled Li/Li–Sn composite electrode was further investigated by using time-of-flight-secondary ion mass spectrometry (TOF-SIMS) depth etching. As shown in Figure 3h and Figure S19 (Supporting Information), the results suggested that this hybrid SEI contains abundant lithium inorganics, including LiF, Li_2CO_3, Li_3N, and some organic oligomers, as reflected by the 3D distribution of Li_3N^-, LiF_2^-, LiO^-, and C_3H^-, respectively, which was consistent with the XPS results. The signal of Sn^- remains weak even after depth etching (Figure S20, Supporting Information), this was in consistent with the EDX results that Li–Sn alloy particles showed good adhesion to the electrode after cycling. The electrochemical cycling of Li/Li–Sn electrode was obtained in the carbonate electrolyte, the SEM of Li/Li–Sn electrode showed a dense and uniform surface after 20 cycles (Figure S21, Supporting Information), indicating the homogenous lithium plating/stripping performance. Therefore, the high lithiophilicity of Li–Sn species distributed in the ultrathin lithium is responsible for the uniform nucleation and the following anisotropic growth of Li grains.

To realize high energy density of batteries, the practicability of the as-fabricated ultrathin Li/Li–Sn electrode was further evaluated in full cell configuration. Ultrathin Li/Li–Sn electrode was paired with $LiFePO_4$ (LFP) electrode with high mass loading (≈2.2 mA h cm^{-2}) to construct LFP||Li/Li–Sn full cells. The N/P ratio can be adjusted from 1.3 to 2.7 by using ultrathin Li/Li–Sn electrodes with different thicknesses, corresponding to areal capacities from 3 to 6 mA h cm^{-2} (15-30 μm). As shown in **Figure 4**a, the cells with Li/Li–Sn electrode exhibited a prolonged lifespan of >300 cycles at 0.5 C, and the discharge capacity remained above 140 mA h g^{-1} with a steady

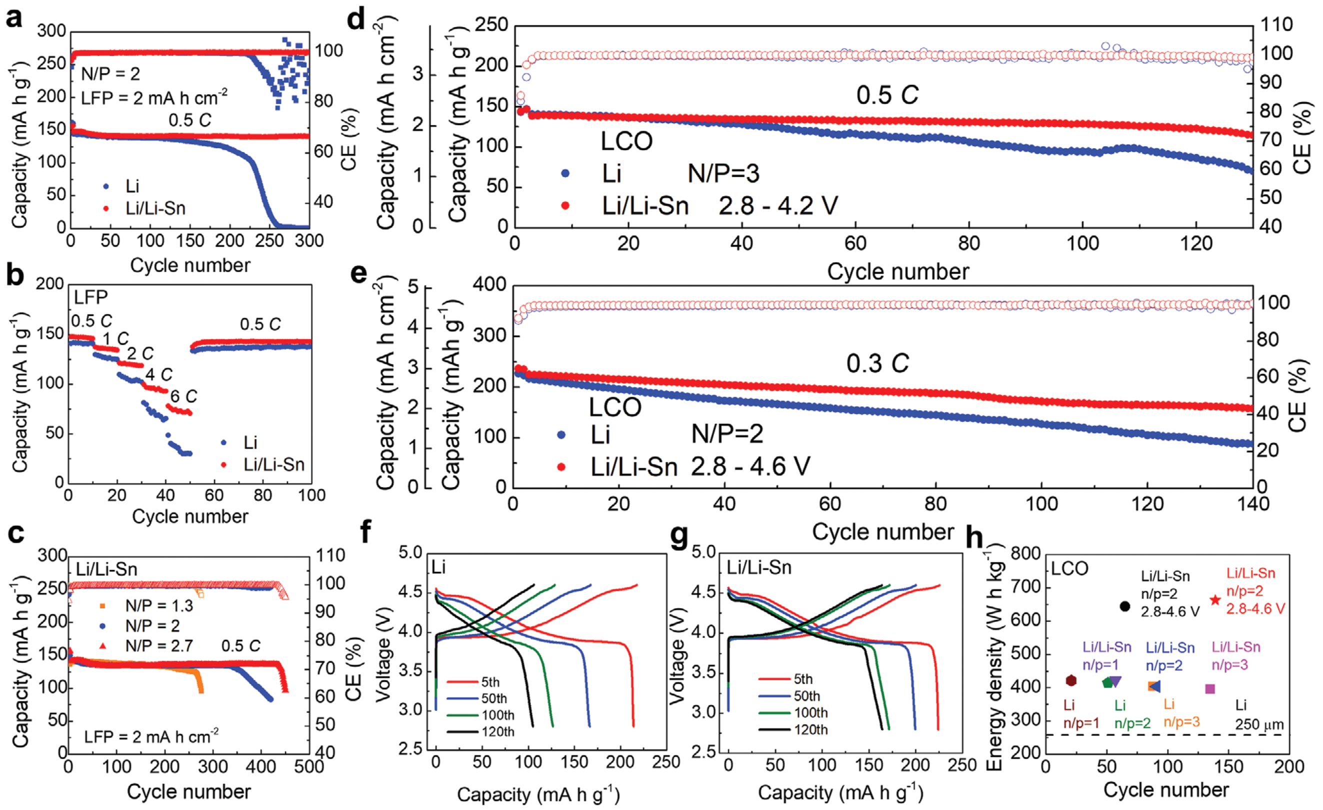

Figure 4. a) Electrochemical performance of LFP||Li and LFP||Li/Li–Sn full cells with N/P ratio of 2/1. b) Cycling performance of LFP||Li and LFP||Li/Li–Sn full cell at different rates. c) Cycling stability of LFP||Li/Li–Sn full cells with different N/P ratios. d) Cycling performance of the LCO||Li and LCO||Li/Li–Sn full cells with a cut-off charge voltage of 4.2 V and N/P ratio of 3/1. e) Cycling performance of the LCO||Li and LCO||Li/Li–Sn full cells with a cut-off charge voltage of 4.6 V and N/P ratio of 2/1. The corresponding voltage profiles of f) LCO||Li and g) LCO||Li/Li–Sn cells. h) Comparison of the energy density and cycling stability of LCO||Li and LCO||Li/Li–Sn cells at different N/P ratios.

CE of nearly 100%. In contrast, the counterpart with ultrathin bare Li anode faded quickly after 150 cycles (Figure S22, Supporting Information). When the N/P ratio increased to 2.7, the LFP||Li–Sn full cell possessed stable cycling of over 400 cycles with a high capacity retention of 97%, while the discharge capacity of the counterpart with bare Li anode dropped quickly after 200 cycles (Figure S23, Supporting Information). The rate capability of LFP||Li/Li–Sn full cells was evaluated to verify the superior kinetics of Li/Li–Sn electrode. The LFP||Li cell offered capacities of 140.6 mA h g^{-1} at 0.5 C, 126.8 mA h g^{-1} at 1 C, 103.8 mA h g^{-1} at 2 C, 70.1 mA h g^{-1} at 4 C, and 33.8 mA h g^{-1} at 6 C, respectively. In comparison, the LFP||Li/Li–Sn cell possessed increased capacities at all tested current densities, such as 147.3 mA h $^{-1}$g at 0.5 C, 136.2 mA h g^{-1} at 1 C, 120.2 mA h g^{-1} at 2 C, 95.9 mA h g^{-1} at 4 C, and 73.7 mA h g^{-1} at 6 C, respectively (Figure 4b and Figure S24, Supporting Information). A typical charge/discharge curve of LFP full cells at a rate capability of 1 C was shown in Figure S25 (Supporting Information). The voltage hysteresis of LFP||Li/Li–Sn was 0.18 V, which was much lower than that of the LFP||Li cell (0.29 V), indicating the fast kinetics of lithium plating/stripping behaviors of the Li/Li–Sn electrode. The improvement in kinetics of Li/Li–Sn electrode is well corroborated by the above results that the Li/Li–Sn electrode delivered a larger exchange current density and afforded amounts of lithiophilic Li–Sn sites for uniform lithium deposition. Figure 4c showed the electrochemical performance of the LFP||Li/Li–Sn full cells with different N/P ratios. With the increase of N/P ratios, the lifespan of the full cells was prolonged from 270 to 400 cycles, much better than the counterparts with pure Li anodes (Figure S26, Supporting Information). The energy density of the LFP||Li/Li–Sn full cells with different N/P ratios were calculated based on the total mass of the cathode and anode. As shown in Figure S27 (Supporting Information), the LFP||Li/Li–Sn full cells possessed high energy density of 366 W h kg^{-1} at a N/P ratio of 2/1. The full cells with Li/Li–Sn anode also exhibited prolonged lifespan than the cell with pure Li anode. Although the employ of thick Li anode could greatly improve the cycling lifespan of full cells, the energy density would significantly decrease due to the excess lithium (for example, as shown in Figure S28 (Supporting Information), the full cell with 250 µm-thick Li metal anode exhibited stable charge/discharge of 200 cycles but extremely low energy density of 223 W h kg^{-1}).

To further investigate the electrochemical performance of Li/Li–Sn electrode, $LiCoO_2$ (LCO)||Li/Li–Sn full cells were also fabricated and measured. With a high areal capacity of about 2 mA h cm^{-2} for the LCO cathode, both LCO||Li and LCO||Li/Li–Sn full cells showed increased lifespan with the increase of N/P ratio from 1/1 to 3/1 (Figure S29 (Supporting Information), corresponding to anodes with thicknesses from 10 to 30 µm).

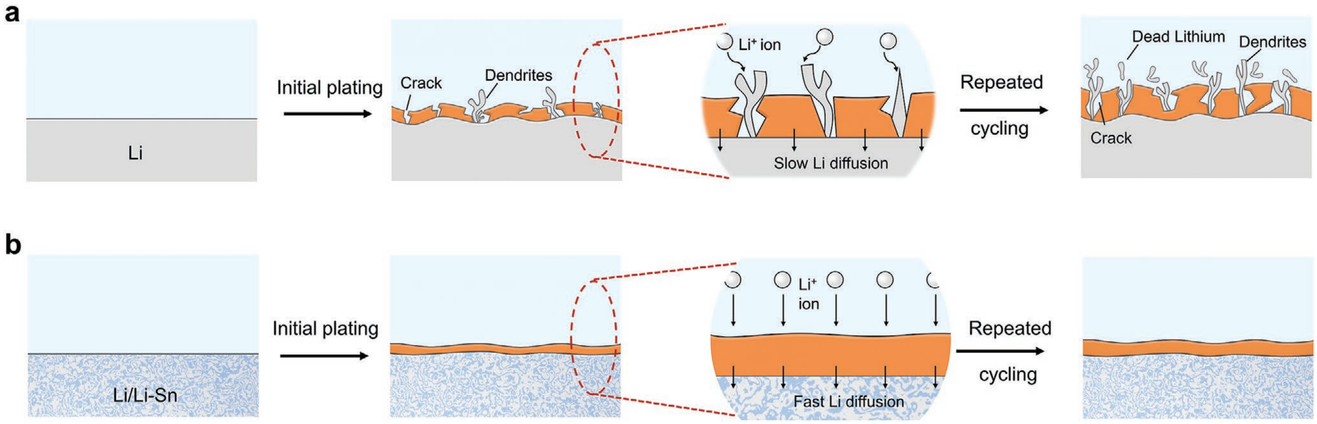

Figure 5. Schematic illustration of lithium plating/stripping behaviors of a) bare Li and b) Li/Li–Sn electrodes.

Typically, as shown in Figure 4d and Figure S30 (Supporting Information), the LCO||Li cell (N/P = 3) exhibited fast capacity decay with 49% capacity retention after 130 cycles at 0.5 C, while the cell with Li/Li–Sn anode showed 83% capacity retention under the same test condition, suggesting much improved cycling stability. The fast capacity decay of LCO||Li cell is mainly caused by the fast lithium exhaustion of the bare Li. With a potential window between 2.8 and 4.6 V, the LCO||Li/Li–Sn full cell possessed a high specific capacity of ≈200 mA h g^{-1} at 0.3 C with a low N/P ratio of 2/1 and high capacity retention of 77% was achieved after 100 cycles (Figure 4e). In contrast, the LCO||Li cell showed continuous capacity decay under the same test condition, with only 55% of capacity retention after 100 cycles. As shown in Figure 4f,g, LCO||Li/Li–Sn cell exhibited smaller voltage hysteresis than LCO||Li cell, which could be attributed to the continuous increased amount of SEI and dead lithium, and consumption of electrolyte.[10f,16] Electrochemical impedance spectroscopy (EIS) measurement was conducted to verify the above results. The cell with Li/Li–Sn anode displayed much smaller R_{SEI} than the counterpart with bare Li anode after 140 cycles (58 Ω for LCO||Li/Li–Sn versus 182 Ω for LCO||Li), indicating the improved stability of electrode/electrolyte interface for the Li/Li–Sn anode during repeated cycling (Figure S31, Supporting Information). The LCO||Li/Li–Sn also showed excellent cycling stability under lean electrolyte condition with an electrolyte/cathode ratio of 12 µL (mA h)$^{-1}$, and presented 68% capacity retention after 100 cycles (Figure S32, Supporting Information). The energy density of the LCO||Li/Li–Sn full cell was also calculated. The cell delivered a high energy density of 394.9 W h kg^{-1} in the voltage range of 2.8–4.2 V, as well as a prolonged lifespan of over 130 cycles. A higher energy density of 662.9 W h kg^{-1} was achieved when the cutoff voltage increased to 4.6 V, much higher than the cell with bare Li metal anode. (Figures S33 and S34, Supporting Information).

In terms of the above results demonstrated, the deposition behaviors of Li on the bare Li electrode and Li/Li–Sn electrode are illustrated as a schematic diagram in **Figure** 5. For the bare Li electrode, due to the larger lithium nucleation overpotential, lithium metal tends to deposit at the random "hot spots."[17] Due to the "tip effect," lithium dissolution and deposition takes place at these specific sites in the stripping/plating process. In the following cycles, continuous deposition and dissolution behavior also occurs at these sites.[5a,18] Besides, the slow lithium diffusion kinetics intensifies the nonuniform deposition of lithium. Such uneven deposition/dissolution behaviors would induce the formation of dendritic morphology, and even the generation of "dead lithium," eventually resulting in the formation of porous, loose surface layer. The high accessible surface of the deposited Li to the liquid electrolyte over cycling would lead to fast consumption of the electrolyte and active Li during cycling, and formation of abundant SEI, which cause low CE for Li cycling. By contrast, the lithiophilic nature of uniformly dispersed Li–Sn sites in Li/Li–Sn alloy decreased the lithium nucleation barrier, and the large chemical diffusion coefficient of Li–Sn alloy ensures the fast lithium diffusion over the entire electrode, thus avoiding the generation of large protrusions and producing uniform and dense deposition layer, and improving the CE for Li cycling. Therefore, high energy density and stable cycling of batteries can be synchronously realized due to the uniform lithium plating/stripping behavior of the ultrathin Li/Li–Sn electrode.

3. Conclusions

In summary, we developed a simple strategy for the fabrication of ultrathin Li/Li–Sn metal electrode and investigated the mechanism behind the superior electrochemical performance. With the assistance of lithiophilic Sn coating, an ultrathin Li/Li–Sn electrode with controlled areal capacities was easily obtained by a facile molten metal doctor-blade casting approach. Compared to bare Li electrode, the ultrathin Li/Li–Sn anode showed uniform lithium deposition behavior, effectively suppressing the dendrite growth and improving the CE during cycling. As a result of the priority demonstrated above, the 25 µm-thick ultrathin Li/Li–Sn electrode exhibited excellent electrochemical performance, offering 900 h stable cycling at 1 mA cm^{-2} and 1 mA h cm^{-2}. Moreover, by pairing with LCO cathode with high areal capacity (2.7 mA h cm^{-2}), the full cell displayed a high discharge capacity of 160 mA h g^{-1} after 140 cycles at a low N/P ratio of 2/1. The ultralow mass loading of the Li/Li–Sn electrode enabled the full cell to realize a high energy density of 662.4 W h kg^{-1}.

4. Experimental Section

Synthesis of Cu/Sn Substrate: Cu foils were cleaned by acetone and ethanol, repeatedly, and dried in vacuum. A thin and uniform Sn nanolayer (≈0.2 mg cm^{-2}) was sputtered on the as-cleaned Cu foils by using a DENTON VACUUM Explorer-14 magnetron sputtering device.

Synthesis of Ultrathin Li/Li–Sn Anode: The fabrication of ultrathin Li/Li–Sn electrode was realized in an Ar-filled glove box. The as-prepared Cu/Sn foil was heated to 200 °C, and then quantitative Li metal (2–10 mA h cm^{-2}) was molted and spread using doctor-blade casting approach. Due to the good affinity of Li to Sn/Li–Sn alloy, Li–Sn alloy was first formed on the surface of Cu foils, and an ultrathin and uniform Li layer was realized on the Li–Sn/Cu surface.

Electrode Fabrication: LFP and LCO electrodes were prepared by mixing active materials, carbon black and polyvinylidene fluoride (PVDF) in *N*-methyl pyrrolidinone (NMP) solvent with a mass ratio of 8:1:1, followed by slurry coating and drying. The active mass loading of LFP and LCO were ≈14 mg cm^{-2} and 12.5–15.5 mg cm^{-2}, respectively.

Material Characterization: Powder XRD measurements were carried out on an Empyrean diffractometer with Cu-Kα radiation source (λ = 1.5406 Å). Before the XRD measurement, the active samples were covered with a Kapton tape for protection. SEM measurements were conducted on a Nova NanoSEM 450 device. XPS was performed to analyze the surface components of cycled Li/Li–Sn electrode on an AXIS-ULTRA DLD-600W instrument. TOF-SIMS was conducted using an ION-TOF (Gmhb 5, Münster, Germany) with an Ar-ion beam.

Electrochemical Measurements: To investigate the electrochemical behavior of the as-prepared ultrathin Li electrodes, Li||Li symmetrical cells, LFP||Li full cells, Li||Cu cells, and LCO||Li full cells were assembled in argon atmosphere. The discharge/charge measurements were conducted on a Neware Battery system. The electrolyte for Li||Li symmetrical cells and LFP||Li full cells was 1.0 м lithium bis(trifluoromethanesulphonyl) imide (LiTFSI) in 1,3-dioxolane (DOL)/1,2-dimethoxyethane (DME) (v/v = 1:1) with 2.0 wt% LiNO$_3$ additive (Dodo Chem). For LCO||Li full cells and Cu||Li cells, the involved electrolyte was 1.0 м lithium hexafluorophosphate (LiPF$_6$) in ethylene carbonate (EC)/dimethyl carbonate (DMC)/ethyl methyl carbonate (EMC) (v/v/v = 1:1:1) with 5% fluoroethylene carbonate (FEC) additive (Dodo Chem). The amount of electrolyte for each cell was 50 µL. A Celgard 2300 membrane was used as the separator. EIS measurement was conducted in the range from 200 kHz to 0.1 Hz at the open-circuit potential. The Tafel curves of Li||Li symmetrical cells were measured at a scan rate of 1 mV s^{-1} from -0.15 to 0.15 V. The exchange current density was calculated based on Tafel equation. The lithium diffusion coefficient of Li–Sn alloy was measured by GITT. The Li–Sn||Li cell was discharged/charged at a current density of 5 µA for 10 min, followed by an open circuit relaxation for 50 min, and such process was repeatedly conducted. The lithium diffusion coefficient was calculated based on the following equation:

$$D_{Li} = \frac{4}{\pi\tau}\left(\frac{n_m V_m}{S}\right)^2\left(\frac{\Delta E_s}{\Delta E_t}\right)^2 \tag{2}$$

where τ (s) is the relaxation time, n_m (mol), and V_m (cm^3 mol^{-1}) are the molar mass and volume of Li–Sn, S is the electrode surface area, ΔE_s (V) is the voltage variation during current pulse, and ΔE_t (V) is the voltage change during the discharge/charge processes.

Supporting Information

Supporting Information is available from the Wiley Online Library or from the author.

Acknowledgements

J.D. and W.W. contributed equally to this work. This work was supported by the National Natural Science Foundation of China (Grant No. 51802105) and Innovation Fund of Wuhan National Laboratory for Optoelectronics. The authors would like to thank the Analytical and Testing Center of Huazhong University of Science and Technology as well as the Center for Nanoscale Characterization & Devices of Wuhan National Laboratory for Optoelectronics for providing the facilities to conduct the characterization.

Conflict of Interest

The authors declare no conflict of interest.

Data Availability Statement

The data that support the findings of this study are available from the corresponding author upon reasonable request.

Keywords

doctor-blade casting, high energy density, stable cycling, ultrathin electrodes, uniform lithium plating/stripping

Received: July 24, 2021
Revised: September 22, 2021

---

[1] a) J.-M. Tarascon, M. Armand, *Nature* **2001**, *414*, 359; b) M. Armand, J.-M. Tarascon, *Nature* **2008**, *451*, 652; c) J. B. Goodenough, K. S. Park, *J. Am. Chem. Soc.* **2013**, *135*, 1167; d) V. Etacheri, R. Marom, R. Elazari, G. Salitra, D. Aurbach, *Energy Environ. Sci.* **2011**, *4*, 3243; e) J. B. Goodenough, Y. Kim, *Chem. Mater.* **2010**, *22*, 587.

[2] a) G. F. Ge, G. C. Li, X. C. Wang, X. X. Chen, L. Fu, X. X. Liu, E. Y. Mao, J. Liu, X. L. Yang, C. X. Qian, Y. M. Sun, *Nano Lett.* **2021**, *21*, 3127; b) W. W. Liu, J. Liu, M. H. Zhu, W. Y. Wang, L. Wang, S. X. Xie, L. Wang, X. L. Yang, X. M. He, Y. M. Sun, *ACS Appl. Mater. Interfaces* **2020**, *12*, 57055; c) J. F. Ding, R. Xu, N. Yao, X. Chen, Y. Xiao, Y. X. Yao, C. Yan, J. Xie, J. Q. Huang, *Angew Chem., Int. Ed. Engl.* **2021**, *60*, 11442; d) R. Zhang, X. R. Chen, X. Chen, X. B. Cheng, X. Q. Zhang, C. Yan, Q. Zhang, *Angew. Chem., Int. Ed. Engl.* **2017**, *56*, 7764; e) H. Ling, L. Shen, Y. Huang, J. Ma, L. Chen, X. Hao, L. Zhao, F. Kang, Y. B. He, *ACS Appl. Mater. Interfaces* **2020**, *12*, 56995; f) W. Ping, C. W. Wang, R. L. Wang, Q. Dong, Z. W. Lin, A. H. Brozena, J. Q. Dai, J. Luo, L. B. Hu, *Sci. Adv.* **2020**, *6*, eabc8641.

[3] a) H. J. Peng, J. Q. Huang, X. B. Cheng, Q. Zhang, *Adv. Energy Mater.* **2017**, *7*, 1700260; b) X. B. Cheng, R. Zhang, C. Z. Zhao, Q. Zhang, *Chem. Rev.* **2017**, *117*, 10403; c) W. Xu, J. L. Wang, F. Ding, X. L. Chen, E. Nasybulin, Y. Zhangad, J. G. Zhang, *Energy Environ. Sci.* **2014**, *7*, 513; d) H. Kim, G. Jeong, Y. U. Kim, J. H. Kim, C. M. Parke, H. J. Sohn, *Chem. Soc. Rev.* **2013**, *42*, 9011; e) X. G. Miao, H. Y. Wang, R. Sun, C. X. Wang, Z. W. Zhang, Z. Q. Li, L. W. Yin, *Energy Environ. Sci.* **2020**, *13*, 3780; f) D. C. Lin, Y. Y. Liu, Y. Cui, *Nat. Nanotechnol.* **2017**, *12*, 194.

[4] a) J. Liu, Z. N. Bao, Y. Cui, E. J. Dufek, Q. Y. Li, B. Y. Liaw, P. Liu, V. R. Subramanian, J. Xiao, W. Xu, J. H. Yang, M. F. Toney, J. B. Goodenough, X. Q. Yang, J. G. Zhang, *Nat. Energy* **2019**, *4*, 180; b) P. Albertus, S. Babinec, S. Litzelman, A. Newman, *Nat. Energy* **2017**, *3*, 16.

[5] a) P. Bai, J. Li, F. R. Brushett, M. Z. Bazant, *Energy Environ. Sci.* **2016**, *9*, 3221; b) H. J. Chang, A. J. Ilott, N. M. Trease, M. Mohammadi, A. Jerschow, C. P. Grey, *J. Am. Chem. Soc.* **2015**, *137*, 15209; c) X. F. Wang, M. H. Zhang, J. Alvarado, S. Wang, M. Sina, B. Y. Lu, J. Bouwer, W. Xu, J. Xiao, J. G. Zhang, J. Liu, Y. S. Meng, *Nano Lett.* **2017**, *17*, 7606.

[6] a) X. R. Li, Y. Tian, L. Shen, Z. B. Qu, T. Q. Ma, F. Sun, X. Y. Liu, C. Zhang, J. Q. Shen, X. Y. Li, L. N. Gao, S. X. Xiao, T. F. Liu, Y. Liu, Y. F. Lu, *Adv. Funct. Mater.* **2021**, *31*, 2009718; b) Y. L. Wang, F. M. Liu, G. L. Fan, X. .G. Qiu, J. D. Liu, Z. H. Yan, K. Zhang, F. Y. Cheng, J. Chen, *J. Am. Chem. Soc.* **2021**, *143*, 2829; c) T. Ma, T. Y. Su, L. Zhang, J. W. Yang, H. B. Yao, L. L. Lu, Y. F. Liu, C. X. He, S. H. Yu, *Nano Lett.* **2021**, *21*, 2347; d) C. Wu, F. H. Guo, L. Zhuang, X. P. Ai, F. P. Zhong, H. X. Yang, J. F. Qian, *ACS Energy Lett.* **2020**, *5*, 1644; e) W. D. Zhang, Z. Y. Shen, S. Y. Li, L. Fan, X. Y. Wang, F. Chen, X. X. Zang, T. Wu, F. Y. Ma, Y. Y. Lu, *Adv. Funct. Mater.* **2020**, *30*, 2003800; f) L. Fu, X. C. Wang, L. Wang, M. T. Wan, Y. J. Li, Z. Cai, Y. C. Tan, G. C. Li, R. M. Zhan, Z. W. Seh, Y. M. Sun, *Adv. Funct. Mater.* **2021**, *31*, 2010602; g) Y. J. Li, W. Y. Wang, X. X. Liu, E. Y. Mao, M. T. Wang, G. X. Li, L. Fu, Z. Li, A. Y. S. Eng, Z. W. Seh, Y. M. Sun, *Energy Storage Mater.* **2019**, *23*, 261; h) K. Shen, Z. Wang, X. X. Bi, Y. Ying, D. Zhang, C. B. Jin, G. Y. Hou, H. Z. Cao, L. K. Wu, G. Q. Zheng, Y. P. Tang, X. Y. Tao, J. Lu, *Adv. Energy Mater.* **2019**, *9*, 1900260.

[7] a) C. Xu, Z. Ahmad, A. Aryanfar, V. Viswanathan, J. R. Greer, *Proc. Natl. Acad. Sci. USA* **2017**, *114*, 57; b) C. D. Fincher, D. Ojeda, Y. Zhang, G. M. Pharr, M. Pharr, *Acta Mater.* **2020**, *186*, 215.

[8] a) J. L. Gao, C. J. Chen, Q. Dong, J. Q. Dai, Y. G. Yao, T. Y. Li, A. Rundlett, R. L. Wang, C. W. Wang, L. B. Hu, *Adv. Mater.* **2021**, *33*, 2005305; b) Z. H. Li, Q. He, C. Zhou, Y. Li, Z. H. Liu, X. F. Hong, X. Xu, Y. Zhao, L. Q. Mai, *Energy Storage Mater.* **2021**, *37*, 40; c) X. Wang, K. Xu, L. Ke, Q. Zhang, D. Jin, H. Shang, K. Rui, Y. Yan, H. Lin, J. Zhu, *ACS Appl. Mater. Interfaces* **2021**, *13*, 16594; d) L. Tan, X. L. Li, T. C. Liu, X. H. Li, *J. Power Sources* **2020**, *463*, 228157.

[9] S. H. Wang, J. P. Yue, W. Dong, T. T. Zuo, J. Y. Li, X. L. Liu, X. D. Zhang, L. Liu, J. L. Shi, Y. X. Yin, Y. G. Guo, *Nat. Commun.* **2019**, *10*, 4930.

[10] a) Z. S. Wang, Z. M. Xu, X. J. Jin, J. H. Li, Q. S. Xu, Y. N. Chong, C. C. Ye, W. S. Li, Y. C. Qiu, *J. Mater. Chem. A* **2020**, *8*, 9218; b) M. T. Wan, S. J. Kang, L. Wang, H. W. Lee, G. Y. W. Zheng, Y. Cui, Y. M. Sun, *Nat. Commun.* **2020**, *11*, 829; c) R. Pathak, K. Chen, A. Gurung, K. M. Reza, B. Bahrami, J. Pokharel, A. Baniya, W. He, F. Wu, Y. Zhou, K. Xu, Q. Q. Qiao, *Nat. Commun.* **2020**, *11*, 93; d) S. Jin, Y. D. Ye, Y. J. Niu, Y. S. Xu, H. C. Jin, J. X. Wang, Z. W. Sun, A. M. Cao, X. J. Wu, Y. Luo, H. X. Ji, L. J. Wan, *J. Am. Chem. Soc.* **2020**, *142*, 8818; e) Z. Peng, J. H. Song, L. Y. Huai, H. P. Jia, B. W. Xiao, L. F. Zou, G. M. Zhu, A. Martinez, S. Roy, V. Murugesan, H. Lee, X. Ren, Q. Y. Li, B. Liu, X. L. Li, D. Y. Wang, W. Xu, J. G. Zhang, *Adv. Energy Mater.* **2019**, *9*, 1901764; f) S. S. Liu, Y. L. Ma, Z. X. Zhou, S. F. Lou, H. Huo, P. J. Zuo, J. J. Wang, C. Y. Du, G. P. Yin, Y. Z. Gao, *Energy Storage Mater.* **2020**, *33*, 423; g) Y. Ouyang, C. Cui, Y. P. Guo, Y. Q. Wei, T. Y. Zhai, H. Q. Li, *ACS Appl. Mater. Interfaces* **2020**, *12*, 25818.

[11] Q. Z. Yan, G. Whang, Z. Y. Wei, S. T. Ko, B. S. Dunn, J. Luo, *Appl. Phys. Lett.* **2020**, *117*, 1.

[12] a) Y. Xu, S. Y. Zhao, G. M. Zhou, W. Chen, F. Zhou, Z. Rong, Y. Wu, J. Li, J. H. Guo, Y. G. Zhang, *ACS Appl. Energy Mater.* **2020**, *3*, 2278; b) H. R. Wang, M. Z. Liu, X. S. Wang, W. G. Zhang, Y. X. Che, L. Chen, Y. P. Wu, W. S. Li, *J. Mater. Chem. A* **2020**, *8*, 12045.

[13] a) G. Z. Wang, M. Aubin, A. Mehta, H. J. Tian, J. F. Chang, A. Kushima, Y. Sohn, Y. Yang, *Adv. Mater.* **2020**, *32*, 2003684; b) H. J. Tian, Z. Li, G. X. Feng, Z. Z. Yang, D. Fox, M. Y. Wang, H. Zhou, L. Zhai, A. Kushima, Y. G. Du, Z. X. Feng, X. N. Shan, Y. Yang, *Nat. Commun.* **2021**, *12*, 237.

[14] a) S. M. Wang, J. Y. Qu, F. Wu, K. Yan, C. Z. Zhang, *ACS Appl. Mater. Interfaces* **2020**, *12*, 8366; b) A. B. Gunnarsd´ottir, S. Vema, L. S. Menkin, E. Marbella, C. P. Grey, *J. Mater. Chem. A* **2020**, *8*, 14975; c) C. Punckt, M. A. Pope, J. Liu, Y. Lin, I. A. Aksay, *Electroanalysis* **2010**, *22*, 2834.

[15] a) H. L. Dai, X. X. Gu, J. Dong, C. Wang, C. Lai, S. H. Sun, *Nat. Commun.* **2020**, *11*, 643; b) C. Y. Cui, C. Y. Yang, N. Eidson, J. Chen, F. D. Han, L. Chen, C. Luo, P. F. Wang, X. L. Fan, C. S. Wang, *Adv. Mater.* **2020**, *32*, 1906427.

[16] S. F. Liu, X. Ji, J. Yue, S. Hou, P. F. Wang, C. Y. Cui, J. Chen, B. W. Shao, J. R. Li, F. D. Han, J. P. Tu, C. S. Wang, *J. Am. Chem. Soc.* **2020**, *142*, 2438.

[17] B. S. Vishnugopi, F. Hao, A. Verma, P. P. Mukherjee, *ACS Appl. Mater. Interfaces* **2020**, *12*, 23931.

[18] Z. Shen, W. Zhang, S. Li, S. Mao, X. Wang, F. Chen, Y. Lu, *Nano Lett.* **2020**, *20*, 6606.